THE JOURNAL OF PHYSICAL CHEMISTRY C
A JOURNAL OF THE AMERICAN CHEMICAL SOCIETY

Zinc Deposition Tuned by Single-Layer Graphene on Copper

Xiaolan Wang, Minghao Guo, Jiahui Xu, Wenshan Jia, Hengxing Ji, Kun Ni,* and Yanwu Zhu*

Cite This: J. Phys. Chem. C 2025, 129, 2317−2324 Read Online

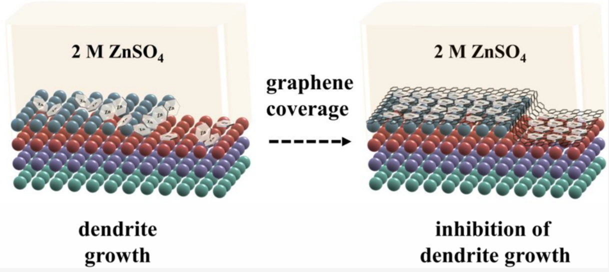

ABSTRACT: Using carbon as a substrate or scaffold has been considered as an efficient strategy to improve the uniformity of zinc deposition, which may boost the anode performance of metal zinc batteries. However, the essential role of the carbon substrate remains unclear. Here, single-layer graphene grown on copper is used as a model material to investigate the interaction between zinc and carbon. The morphology and crystallinity of early-stage zinc deposition with galvanostatic or potentiostatic electrochemical plating are discussed. By using an electrochemical quartz crystal microbalance study, we verify the difference in energy dissipation of the zinc deposition with or without single-layer graphene. Density functional theory simulations show that the presence of graphene reduces the difference in the binding energy of zinc on different sites of defective copper surfaces, thus improving the uniformity of zinc electrodeposition. Our study shows that single-layer graphene can act as the passivation layer of copper to reduce the probability of dendrite growth.

■ INTRODUCTION

Nowadays, lithium ion batteries have been widely used in electronic devices, electric vehicles, large-scale energy storage stations, and so on.[1] However, the disadvantages of lithium ion batteries, e.g., limited lithium resources,[2] instability of lithium in the presence of trace amounts of water vapor,[3] and the usage of toxic nonaqueous electrolytes,[4,5] have pushed one to develop nonlithium batteries.[6] Compared to batteries working with organic electrolytes, batteries with nontoxic and nonflammable aqueous electrolytes would have lower cost, higher safety, better environmental friendship, and faster kinetics in many situations.[7−11] For example, the ionic conductivity of an aqueous electrolyte, composed of 3.86 mol/L (M) calcium chloride and 1 M sodium perchlorate ($NaClO_4$), reaches 390.74 mS/cm at room temperature.[12] By introducing 4 M calcium perchlorate into 1 M $NaClO_4$, the electrolyte can work at a low temperature of −85 °C.[13] Meanwhile, studies have shown that the voltage window of aqueous electrolytes can be increased to 4.5 V by adding acetonitrile as a cosolvent, which dissolves lithium bis(trifluoromethane sulphonyl)imide from water.[14] Among metallic zinc (Zn) aqueous batteries, which have a low redox potential (−0.763 V vs standard hydrogen electrode),[15] a high overpotential of hydrogen evolution reaction (HER)[16] and a reasonably high theoretical energy density (~624.5 Wh kg^{-1}) have been intensive research focuses.

However, like many other metal batteries, aqueous Zn batteries often face the problem of cycling stability, which is caused by dendrite growth. The dendrite growth is much related to the deposition of Zn on Zn (101) and (100) planes, forming vertically aligned flakes, which is quite different from the parallelly aligned growth on the Zn (002) plane.[17] The deeper reason can be ascribed to the different adsorption energy of Zn atoms on the Zn (100) or Zn (002) plane.[18] For the uniform Zn deposition, studies have been performed to promote the deposition on the (002) plane yet suppress the growth on other planes. For example, Liu et al. applied a fluorapatite aerogel interfacial layer on Zn foil to inhibit the migration of Zn ions (Zn^{2+}) to the Zn (101) plane, thus inducing the preferential development of (002) crystals.[19] Wang et al. used (002)-exposed Zn foils as the substrate and efficiently prohibited the growth of dendrites.[20] On the other hand, optimizing the electrolyte could also modulate the deposition behavior of Zn. Wang et al. added sericin molecules into 2 M zinc sulfate ($ZnSO_4$), and the formation of a solid electrolyte interface has refined the diffusion of Zn^{2+} for the reduced growth of dendrites.[21] Bai et al. added amphiphilic choline bromine to 3 M $ZnSO_4$ and found that the distribution of electric field on Zn has been modified, benefiting the preferential deposition on Zn (002).[22] Clearly, regulating substrates and electrolytes is effective for the formation of flat Zn deposition and the suppression of dendrite growth.

Further down to the layer under the Zn foil, copper (Cu) has been commonly used as a current collector, but the multiple crystal facets of polycrystalline Cu have led to the preferential deposition of Zn on certain Cu facets[23] and side reactions like HER.[24] To modify the surface of Cu, an

Received: October 1, 2024
Revised: December 4, 2024
Accepted: December 19, 2024
Published: January 27, 2025

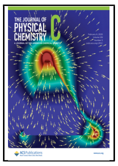

https://doi.org/10.1021/acs.jpcc.4c06348

additional layer such as pyrolyzed polytetrafluoroethylene has been utilized to cover Cu for more zincophilic sites.[25] As a relatively inert and electron-conjugated surface, graphene has been found useful to construct a more proper electrode−electrolyte interface for modulating the Zn deposition. It was reported that the exceptionally high reversibility of Zn deposition was achieved on a few-layer graphene membrane with a lattice mismatch of about 7% between (002) Zn and graphene.[26] The compact Zn pallets were deposited on an ∼120 nm-thick nitrogen-doped graphene oxide on the Cu substrate.[27] It was shown that the coverage of Cu with defective graphene allows for a dendrite-free growth of Zn deposition owing to the stronger affinity between Zn and defects in graphene, compared to the perfect graphene or the bare Cu.[28] Despite the effort toward the more uniform Zn deposition, the detailed mechanisms on how graphene influences the early-stage nucleation of Zn and the subsequent growth remain unclear.

In this work, we take single-layer graphene on copper (SLG@Cu) grown by chemical vapor deposition (CVD) or bare Cu foils as anodes to investigate the influence of SLG on the deposition of Zn. We find that with the galvanostatic (GS) method, the presence of SLG can increase the Zn deposition nucleation overpotential. The *in situ* electrochemical quartz crystal microbalance (EQCM) shows that SLG induces a dense yet flat Zn deposition layer at the initial stage. Under the same high overpotential in potentiostatic (PS) deposition, the Zn crystals deposited on SLG@Cu show more (002) orientations than those on bare Cu. Combining density functional theory (DFT) calculations, SLG is found to have the function of screening the crystal steps and vacancy defects of Cu, thus changing the absorption of Zn^{2+} and leading to the inhibition of dendrite growth at the initial deposition stage, which explains the more homogeneous deposition of Zn on SLG@Cu.

■ METHODS

Sample Preparation and Fabrication of Bare Cu. The SLG grown on Cu (SLG@Cu) was purchased from Ningbo Soft Carbon Electronic Technology Co., Ltd. SLG@Cu was initially cleaned in the tube furnace at 300 °C for 2 h at an argon (Ar) atmosphere with a flow of 100 sccm. To obtain the bare Cu, cleaned SLG@Cu was loaded onto the power electrode of an Oxford Plasma Pro NGP 80 reactive ion etching (RIE) instrument. Ar flow was used to etch SLG, with 100 W power. The etching rate of Cu in Ar flow is reported as nearly as 0 Å /min, even at a power of 1000 W.[29] After RIE in Ar (flow: 50 sccm, pressure: 50 mTorr, time: 6 min)-based plasma was carried out at room temperature, Raman spectroscopy showed that SLG was etched.

Electrochemical Measurements. For electrochemical measurements, SLG@Cu or bare Cu was pasted on clean glass plates with 3 M waterproof silicone tape. A hole with a diameter of 4 mm was opened in the tape to expose the electrode with the electrolyte (2 M $ZnSO_4$, pH ∼4.5). All the electrochemical tests were carried out in a PARSTAT4000 electrochemical workstation equipped with VersaStudio software in a three-electrode cell with a cleaned Zn metal as the counter electrode and Ag/AgCl as the reference electrode. Cyclic voltammetry (CV) was performed at a scan rate of 2 mV/s from −700 mV to 1 V vs Zn^{2+}/Zn. Zn was deposited with a current density of 2 mA/cm^2 or an electrode potential of −540 mV vs Zn^{2+}/Zn. A QSense quartz crystal microbalance instrument with dissipation monitoring was used for electrochemical quartz crystal microbalance measurements.

Characterizations. A HITACHI UHR FE-SEM SU8220 instrument performed with an acceleration voltage of 3 kV and a working distance of 6 mm was used for scanning electron microscopy (SEM). X-ray diffraction (XRD) was conducted on a Rigaku SmartLab diffractometer, with the Cu K_α source operated at 40 kV and 30 mA.

Simulation Methods. DFT calculation was performed with the Vienna Ab initio Simulation Package (VASP).[30] The Perdew−Burke−Ernzerhof (PBE)[31] exchange-correlation functional with a generalized gradient approximation (GGA)[32] was adopted. The van der Waals interactions were described by the DFT-D3 method[33] with Becke−Jonson damping (BJ-D3).[34] The basis set cutoff energy was 400 eV, and the Brillouin zone was sampled using a gamma centered K points grid with K points spacing distance of 0.04 $Å^{-1}$ in structure optimization. The self-consistent field (SCF) calculation was done with an energy convergence criterion of 10^{-4} eV and a force tolerance of 0.05 eV $Å^{-1}$. The simulation cells had a 21.14 × 7.32 Å lattice with a 20.00 Å vacuum layer for Cu (100) and Cu (100) planes with SLG, a 21.14×10.05 Å lattice with a 20.00 Å vacuum layer for Cu (110) andCu (110) planes with SLG, a 8.54×10.05 Å with a 20.00 Å vacuum layer for Cu (111) and Cu (111) planes with SLG.

■ RESULTS AND DISCUSSION

The morphological comparison of deposited Zn at the nucleation step on bare Cu (the SEM image is shown in Figure S1) and SLG@Cu is shown in Figure 1a−d. For the

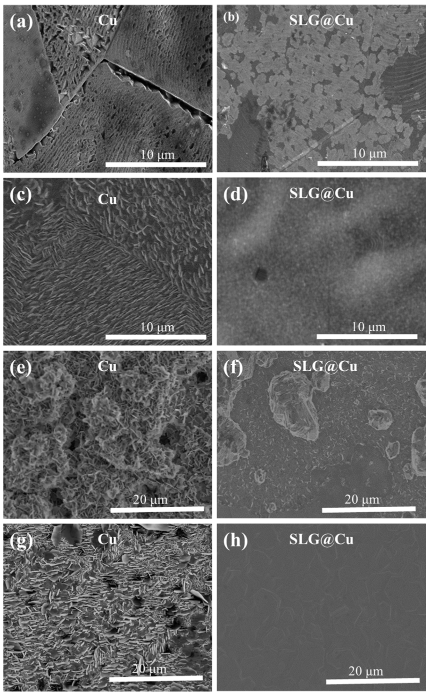

Figure 1. SEM images of Zn deposition on (a) bare Cu and on (b) SLG@Cu by GS deposition at 2 mA/cm^2 for 10 s and on (c) bare Cu and on (d) SLG@Cu by PS deposition at −540 mV for the deposition amount of 20 mAs/cm^2. SEM images of Zn deposition on (e) bare Cu and on (f) SLG@Cu by GS deposition at 2 mA/cm^2 for 1 h and on (g) bare Cu and on (h) SLG@Cu by PS deposition at −540 mV for the amount of 2 mAh/cm^2.

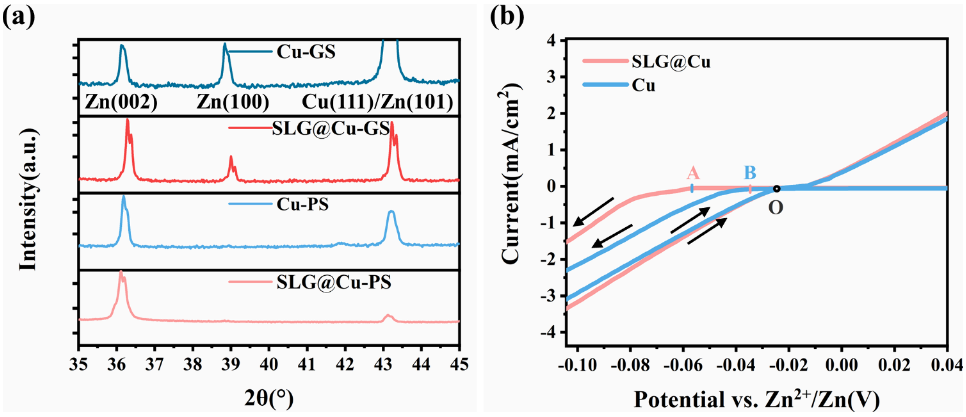

Figure 2. (a) XRD patterns of Zn obtained by two deposition methods yet with the same capacity of 2 mAh/cm^2. PS deposition was carried out at −540 mV vs Zn^{2+}/Zn potential, and GS deposition was carried out at 2 mA/cm^2. (b) CV curves showing the initial plating and stripping process of Zn on Cu or SLG@Cu with a scan rate of 2 mV/s. The black arrows indicate the sweeping directions.

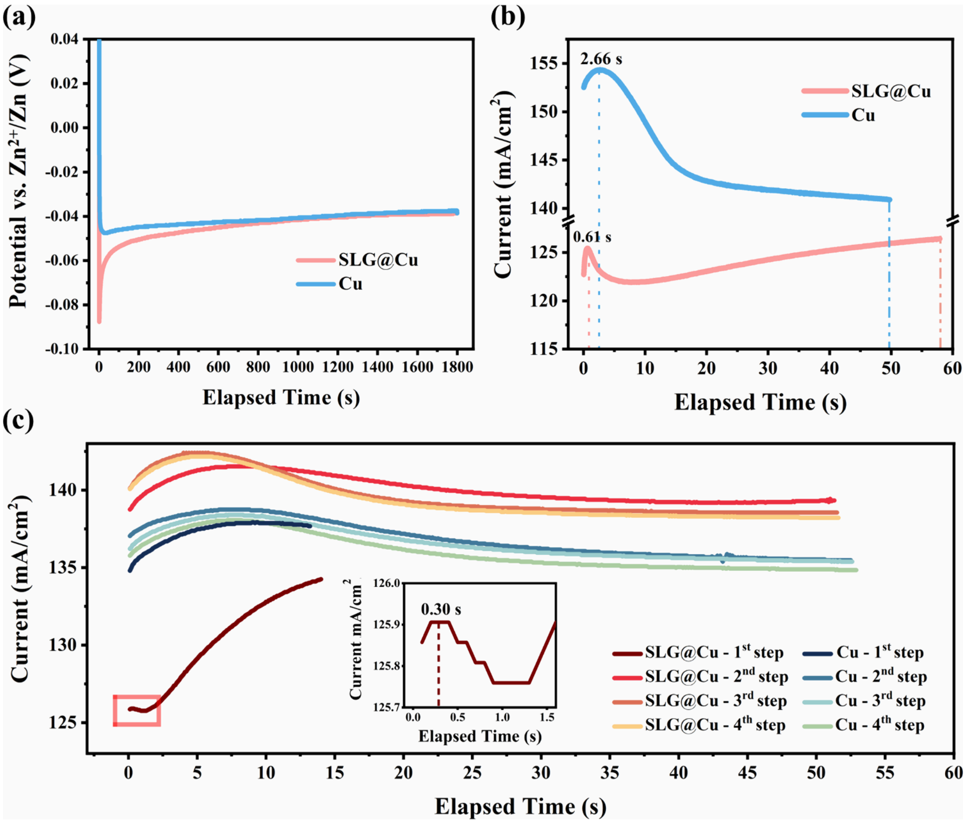

Figure 3. (a) Potential time curves captured in GS deposition performed at 2 mA/cm^2 for 30 min on SLG@Cu or on bare Cu. (b) Current−time curves captured in PS deposition at −540 mV vs Zn^{2+}/Zn on SLG@Cu or on bare Cu, with a deposition capacity of 2 mAh/cm^2. (c) Evolution of current in four-step depositions with an amount of 2 mAh/cm^2 for each by PS deposition performed at −540 mV. Inset: the first step deposition on SLG@Cu within 1.6 s.

deposition, GS (performed at 2 mA/cm^2 for 10 s) or PS (performed at −540 mV until 20 mAs/cm^2) plating was utilized for the same deposition amount of 20 mAs/cm^2 on each substrate. As shown in Figure 1a, from the GS deposition, the morphology of Zn tends to form moss/wrinkle-like structures on the bare Cu foil, which is often regarded as the origin of dendrite growth.[35] Grooves are observed in the Zn deposition layer, which may be related to the stress caused by the uneven polycrystal Cu substrate, as shown in Figure 1a. In contrast, 2D flakes are formed on SLG@Cu by the same GS deposition, showing nucleation spanning multiple crystal steps and grain boundaries of Cu, as shown in Figure 1b. Figure 1c shows that the growth of Zn flakes occurs along the direction perpendicular to the bare Cu surface under the PS deposition condition and is sensitive to the contours of grain boundaries of Cu as well. On the other hand, no vertically aligned Zn flakes are observed on SLG@Cu by the PS deposition, as shown in Figure 1d. Clearly, the SLG@Cu substrate has induced a flatter deposition of Zn, and the PS deposition with a potential of −540 mV can further improve the nucleation uniformity compared with the GS deposition performed at 2 mA/cm^2.

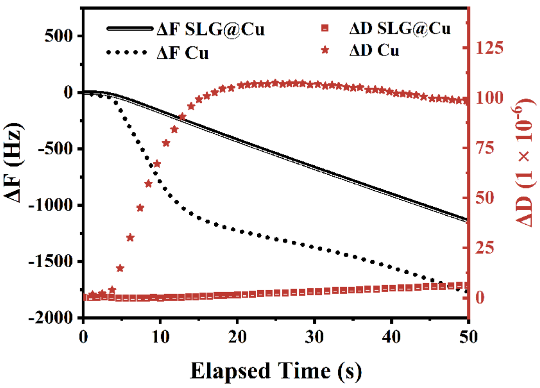

Figure 4. EQCM Δ*F*-time and Δ*D*-time curves captured in the GS deposition performed at 1 mA/cm^2 for 50 s on SLG@Cu or bare Cu.

To further investigate the subsequent growth of Zn deposition, a larger amount of deposition was carried out for 2 mAh/cm^2 by the PS method performed at −540 mV or by the GS method performed at 2 mA/cm^2 for 1 h on the bare Cu or SLG@Cu substrate. Typical SEM images of Zn deposition are shown in Figure 1e−h. Both GS (Figure 1e) and PS (Figure 1g) depositions on the bare Cu lead to lose and porous structures consisting of flake-shape Zn dendrites, which are considered harmful to the long cycling performance.[36] In the case of SLG@Cu, the larger amounts of GS (Figure 1f) and PS (Figure 1h) deposition result in a more uniform surface morphology over a large area. Among the two deposition methods, the Zn layers deposited under PS conditions are smoother and there is no preferential deposition observed.

XRD patterns of deposited Zn from a deposition amount of 2 mAh/cm^2 are shown in Figure 2a, with all peak intensities normalized to the intensity of Zn (002). Herein, we mainly focus on the discussion of the Zn (100) peak, as the Zn (101) and Cu (111) peaks are overlapped. The relative intensity of Zn (100) on Cu deposited by GS plating is 0.9, close to the value of bulk Zn metal (PDF #04-0831). On SLG@Cu, the intensity of Zn (100) reduces to 0.31 for the same GS plating. From the PS plating performed at an overpotential of −540 mV, the intensity of Zn (100) drops to 0.05 for both substrates. The relative intensity of Zn (101) and Cu (111) peaks is significantly reduced when SLG covers the surface of Cu because of the highly oriented Zn (002) crystallization, consistent with previous results.[37,38] The high (002) content of Zn deposition is considered to inhibit the dendrite growth.[39] The CV results are listed in Figure 2b. The crossover of cathodic and anodic current is defined as the *O* point, which is known as the crossover potential.[40] The starting potential for the reduction of Zn^{2+} on SLG@Cu, at −56 mV, is defined as the *A* point, and that for the reduction of Zn^{2+} on bare Cu, at −34 mV, is defined as the *B* point. The potential difference between point *O* and point *A*/*B* is the nucleation overpotential,[41] which is 32 mV for SLG@Cu or 10 mV for bare Cu. The increased overpotential on SLG@Cu causes more Zn nucleation sites, and the nucleation radius is negatively correlated to the overpotential.[42]

The evolution of potential versus time in GS deposition performed at 2 mA/cm^2 is shown in Figure 3a. On SLG@Cu, the potential initially drops to the lowest value of −87 mV vs Zn^{2+}/Zn and then slowly increases to a platform of about −48 mV, resulting in an overpotential of 39 mV. In comparison, on the bare Cu, the potential initially drops to −47 mV and then slightly increases to −43 mV, causing an overpotential of 4 mV. The crystallization theory developed by Budevski et al.[43] could be used to phenomenologically explain the difference, as shown in eq 1:

$$i_{\mathrm{dt}} = L_{\mathrm{s}} d_{\mathrm{o,Me}} i^{\mathrm{local}}_{\mathrm{o,step}} \frac{zF\eta}{RT} \tag{1}$$

where i_{dt} is the current density, L_{s} is the step density, $d_{\mathrm{o,Me}}$ is the spacing between metal atoms, $i^{\mathrm{local}}_{\mathrm{o,step}}$ is the exchange current density at the step sites, z is the charge number of metallic ions, F is the Faraday constant, R is the gas constant, T is the temperature, and η is the overpotential. From eq 1, we can see that when i_{dt} is fixed, the overpotential η is negatively correlated to the step density L_{s}. Therefore, the higher overpotential observed on SLG@Cu corresponds to the lower density of steps on the reaction surface, indicating that the SLG could shield some of the crystal steps and grain boundaries of Cu, resulting in a more homogeneous distribution of the initial deposition.[44]

Figure 3b shows the current evolution captured in PS deposition performed at −540 mV, until a maximum deposition capacity of 2 mAh/cm^2. The current density on both substrates shows a hump at the initial nucleation stage. Within 0.61 s for SLG@Cu or 2.66 s for Cu, the increase in current density is caused by the formation and growth of nuclei, while the subsequent decrease is reasoned by the overlapping of adjacent nuclei, which agrees with the multisite nucleation theory.[45] The time to reach the maximum current density (t_{m}) is related to the density of nuclei (N_0) on the electrode for the instantaneous nucleation, as given in eq 2:

$$t_{\mathrm{m}} = \frac{1}{\sqrt{\pi k_1 N_0}} \tag{2}$$

or the nucleation rate J_0 for the continuous nucleation, as given in eq 3:

$$t_{\mathrm{m}} = \sqrt[3]{\frac{2}{\pi k_2 J_0}} \tag{3}$$

where k_1 and k_2 are constants related to the growth rates of the nuclei.[46] The smaller value of t_{m} on SLG@Cu indicates a higher nucleation density on SLG@Cu and a faster nucleation rate. Khoumri et al. reported that the higher current density on Cu is related to the Langmuir adsorption of Zn to the substrate,[47] which could be explained by the stronger binding of Zn on Cu than that on SLG@Cu.[28] The decreased current density after 2.66 s for Cu is ascribed to the nucleation and growth of Zn, which is controlled by diffusion of ions.[47] The slow increase in current density after the first hump for SLG@Cu may originate from a transition of the growth mode since the behavior of Zn deposition on SLG is quite different from that on as-deposited Zn.

To further track the effect of initial nucleation on the subsequent growth, Zn was deposited in four steps: (i) an initial deposition of 0.5 mAh/cm^2 and (ii−iv) the following deposition of 2 mAh/cm^2 repeated three times. In this way, a cumulative deposition of 6.5 mAh/cm^2 was achieved after all of the steps. The current density evolution during the four-step deposition is shown in Figure 3c. The humps appearing for 0 to ∼20 s in all curves show the agreement with the multisite nucleation theory again.[45] On the bare Cu, the peak position and shape in each curve show no obvious change from the second step to the fourth step. On SLG@Cu, the first step is

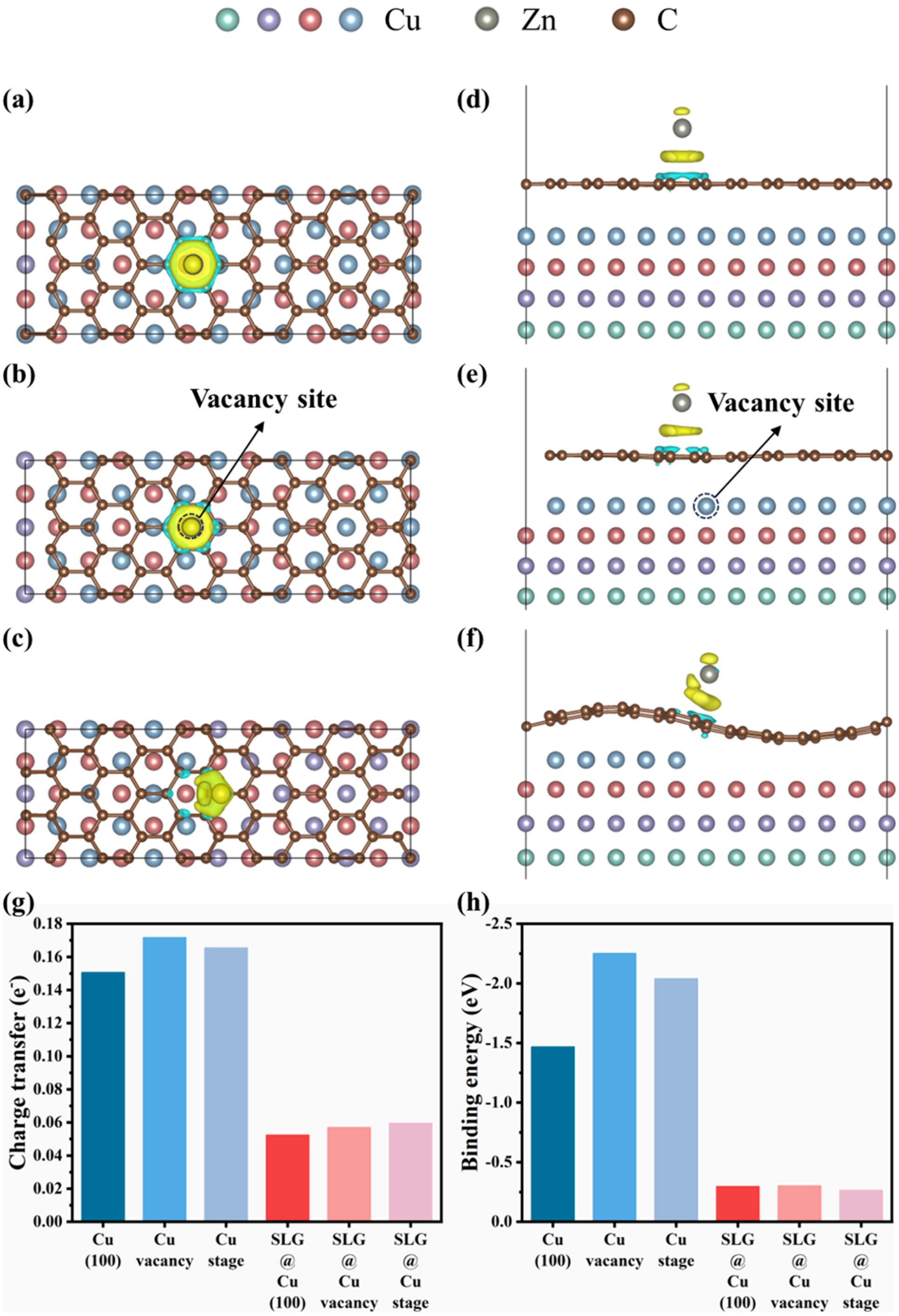

Figure 5. Top view differential charge density distribution for a Zn atom on (a) SLG@Cu (100), (b) SLG@Cu (100) with vacancy, and (c) SLG@Cu (100) with a stage. (d−f) Corresponding side views. The value of the iso-surface is 0.0002 e/bohr^3 for panels (a−f). (g) Charge transfer based on Bader analysis and (h) binding energy between Zn and Cu (100)-related substrates, where the energy of isolated Zn atoms is used.

similar to the initial stage of 2 mAh/cm^2 deposition shown in Figure 3b. The second-step deposition, which obviously occurs on the Zn layer deposited in the first step, shows a broadened peak and higher current density due to the lower Zn diffusion barrier[48] and the lower Zn affinity on SLG@Cu.[49] In the third and fourth depositions, the current maximum is higher and t_m is smaller compared to the second step, caused by the increased size of the electrode rather than the change of nucleation and growth, as reported by Heerman et al.[50] Figure 1a,b shows that the deposition morphology has been influenced by the nucleation in the initial deposition, justifying the role of SLG on the modulation of the Zn deposition behavior at the initial stage.

The EQCM working in the dissipation monitoring mode has been used to detect the viscoelastic characteristics of Zn deposition by testing the frequency decay at quartz resonance.[51] According to the Kanazawa−Gordon equation,[52] when the quartz is covered with a film, the resonance frequency of the sensor (F) is not only related to mass but also related to the rigidity of the film, which affects the energy dissipation at resonance (D). As shown in Figure 4, there is a remarkable difference between the change in F (ΔF) and the change in D (ΔD) between the bare Cu and SLG@Cu for the electrochemical Zn deposition. We can see that the slope of the ΔF-time curve for SLG@Cu is essentially constant, whereas the slope of the curve for bare Cu can be divided into three distinct stages. Correspondingly, the ΔD remains a small yet relatively constant value with time for SLG@Cu, indicating consistent deposition behavior due to the denser Zn deposition and more rigid deposition layer. On bare Cu, the ΔD-time curve can be also divided into three stages corresponding to the three stages in the ΔF-time curve. In the first stage (first 3 s), the deposition has not yet occurred, and the very small difference in ΔF between SLG@Cu and bare Cu may be related to the different ion adsorptions. In the second stage (from 3 to 15 s), the dramatic changes in ΔD and ΔF are related to the initial inhomogeneous nucleation, where the formation of loosely deposited Zn on bare Cu causes lower rigidity and larger energy dissipation. When the dendrite is formed in the third stage (after 15 s), the looseness of the sedimentary layer reaches the maximum and ΔD remains nearly unchanged on bare Cu. The decrease in ΔD may be explained by the connected or merged dendrites as the deposition proceeds.

Density functional theory (DFT) simulations have been performed to verify the role of SLG in Zn deposition. The relative positions of the atoms are shown in Figures S2–S4. Differential charge density, accompanied by Bader charge analysis, is shown in Figure 5a–f (SLG@Cu (100)) and Figure S5 (SLG@Cu (110)), Figure S6 (SLG@Cu (111)), Figure S7 (Cu (100)), Figure S8 (Cu (110)), and Figure S9 (Cu (111)), confirming that the existence of vacancy and stage leads to the stronger electronic interaction between the Zn and Cu surface. As shown in Figure 5g, the charge transfers from Zn to Cu (100) are calculated as 0.171 e^- on the vacancy site, 0.166 e^- on the stage site, and 0.151 e^- on the pristine surface. In comparison, the charge transfer is much weakened when the SLG is covered on Cu. Figure 5h shows the binding energy of Zn on bare Cu (100) or SLG@Cu (100), from which again we can see the enhanced absorption energy (E_{ads}) for Zn on Cu (100) with defective sites, such as vacancy and stage. Due to the much lower electron transfer, the binding energy between Zn and SLG@Cu is largely reduced compared to the situation on bare Cu (100). The charge transfer amounts from Zn to Cu (110) and Cu (111) with vacancy and stage and covered by SLG are also shown in Figure S10. Very importantly, the coverage of SLG on Cu has diminished the difference in E_{ads} between the defective sites and perfect Cu. Therefore, the presence of SLG has screened the interaction between Zn and Cu and weakened the influence of defects in Cu underneath the SLG, if there are any.

■ CONCLUSIONS

In this study, the impact of the SLG covering Cu on Zn deposition has been comprehensively elucidated through electrochemical experiments and DFT simulations. The presence of SLG on Cu has modulated the interaction between Zn and Cu: (i) SLG changes the ion absorption on Cu; (ii) the nucleation overpotential of Zn alters the Zn deposition behavior; (iii) uniform Zn deposition has been achieved under large overpotential on SLG@Cu, with a preference for growth with more (002) orientation on the surface of the electrode. This study provides valuable insight into the mechanism of the morphological control of Zn electrodes and would innovate electrode design for long-life Zn metal batteries.

■ ASSOCIATED CONTENT

Data Availability Statement

All data needed to evaluate the conclusions in the paper are present in the paper and/or the Supporting Information. Additional data related to this paper may be requested from the authors.

Supporting Information

The Supporting Information is available free of charge at https://pubs.acs.org/doi/10.1021/acs.jpcc.4c06348.

> SEM image of the bare Cu foil; side view of the Zn atom on Cu (100), SLG@Cu (100), Cu (110), SLG@Cu (110), Cu (111), and SLG@Cu (111); top view and side view of differential charge density distribution on SLG@Cu (110), SLG@Cu (111), Cu (100), Cu (110), and Cu (111) (PDF)

■ AUTHOR INFORMATION

Corresponding Authors

Kun Ni − *Department of Materials Science and Engineering, School of Chemistry and Materials Science, University of Science and Technology of China, Hefei 230026, China*; Email: nikun@ustc.edu.cn

Yanwu Zhu − *Department of Materials Science and Engineering, School of Chemistry and Materials Science, Hefei National Research Center for Physical Sciences at the Microscale, and Key Laboratory of Precision and Intelligent Chemistry, University of Science and Technology of China, Hefei 230026, China*; orcid.org/0000-0002-7505-1502; Phone: 86-551-63607670; Email: zhuyanwu@ustc.edu.cn

Authors

Xiaolan Wang − *Department of Materials Science and Engineering, School of Chemistry and Materials Science, University of Science and Technology of China, Hefei 230026, China*

Minghao Guo − *Department of Materials Science and Engineering, School of Chemistry and Materials Science, University of Science and Technology of China, Hefei 230026, China*

Jiahui Xu − *Department of Materials Science and Engineering, School of Chemistry and Materials Science, University of Science and Technology of China, Hefei 230026, China*

Wenshan Jia − *Hefei National Research Center for Physical Sciences at the Microscale, University of Science and Technology of China, Hefei 230026, China*

Hengxing Ji − *Hefei National Research Center for Physical Sciences at the Microscale and School of Chemistry and Materials Science, iChEM, University of Science and Technology of China, Hefei 230026, China*; orcid.org/0000-0003-2851-9878

Complete contact information is available at: https://pubs.acs.org/10.1021/acs.jpcc.4c06348

Author Contributions

X.W. and M.G. contributed equally to this work. X.W. performed the experiments, data analysis, and manuscript writing. J.X. helped perform the experiments and data analysis. M.G. performed the simulations. W.J. helped perform the characterization of the EQCM. H.J. gave support on the EQCM. K.N. discussed the data and revised the manuscript. Y.Z. supervised the study and revised the manuscript.

Notes

The authors declare no competing financial interest.

■ ACKNOWLEDGMENTS

This work was supported by the National Key R&D Program of China (grant no. 2020YFA0711502), the Natural Science Foundation of China (nos. 52273234, 52273239, and 52325202) and the Fundamental Research Funds for the Central Universities (WK9990000170). The USTC Center for Micro and Nanoscale Research and Fabrication, the Supercomputing Center of USTC, and the Hefei Advanced Computing Center are appreciated.

■ REFERENCES

(1) Xiao, J.; Shi, F.; Glossmann, T.; Burnett, C.; Liu, Z. From laboratory innovations to materials manufacturing for lithium-based batteries. *Nature Energy* **2023**, *8* (4), 329−339.

(2) Wang, J.; Yue, X.; Wang, P.; Yu, T.; Du, X.; Hao, X.; Abudula, A.; Guan, G. Electrochemical technologies for lithium recovery from liquid resources: A review. *Renewable and Sustainable Energy Reviews* **2022**, *154*, No. 111813.

(3) Li, Y.; Li, Y.; Sun, Y.; Butz, B.; Yan, K.; Koh, A. L.; Zhao, J.; Pei, A.; Cui, Y. Revealing Nanoscale Passivation and Corrosion Mechanisms of Reactive Battery Materials in Gas Environments. *Nano Lett.* **2017**, *17* (8), 5171−5178.

(4) Zhang, J.-G.; Xu, W.; Xiao, J.; Cao, X.; Liu, J. Lithium Metal Anodes with Nonaqueous Electrolytes. *Chem. Rev.* **2020**, *120* (24), 13312−13348.

(5) Xu, K. Electrolytes and Interphases in Li-Ion Batteries and Beyond. *Chem. Rev.* **2014**, *114* (23), 11503−11618.

(6) Tian, Y.; Zeng, G.; Rutt, A.; Shi, T.; Kim, H.; Wang, J.; Koettgen, J.; Sun, Y.; Ouyang, B.; Chen, T.; et al. Promises and Challenges of Next-Generation "Beyond Li-ion" Batteries for Electric Vehicles and Grid Decarbonization. *Chem. Rev.* **2021**, *121* (3), 1623−1669.

(7) Kim, H.; Hong, J.; Park, K.-Y.; Kim, H.; Kim, S.-W.; Kang, K. Aqueous Rechargeable Li and Na Ion Batteries. *Chem. Rev.* **2014**, *114* (23), 11788−11827.

(8) Alias, N.; Mohamad, A. A. Advances of aqueous rechargeable lithium-ion battery: A review. *J. Power Sources* **2015**, *274*, 237−251.

(9) Chao, D.; Qiao, S.-Z. Toward High-Voltage Aqueous Batteries: Super- or Low-Concentrated Electrolyte? *Joule* **2020**, *4* (9), 1846−1851.

(10) Chao, D.; Zhou, W.; Xie, F.; Ye, C.; Li, H.; Jaroniec, M.; Qiao, S.-Z. Roadmap for advanced aqueous batteries: From design of materials to applications. *Science. Advances* **2020**, *6* (21), No. eaba4098.

(11) Wang, H.; Tan, R.; Yang, Z.; Feng, Y.; Duan, X.; Ma, J. Stabilization Perspective on Metal Anodes for Aqueous Batteries. *Adv. Energy Mater.* **2021**, *11* (2), No. 2000962.

(12) Zhu, K.; Li, Z.; Sun, Z.; Liu, P.; Jin, T.; Chen, X.; Li, H.; Lu, W.; Jiao, L. Inorganic Electrolyte for Low-Temperature Aqueous Sodium Ion Batteries. *Small* **2022**, *18* (14), No. 2107662.

(13) Jiang, L.; Han, S.; Hu, Y.-C.; Yang, Y.; Lu, Y.; Lu, Y.-C.; Zhao, J.; Chen, L.; Hu, Y.-S. Rational design of anti-freezing electrolytes for extremely low-temperature aqueous batteries. *Nature Energy* **2024**, *9* (7), 839−848.

(14) Chen, J.; Vatamanu, J.; Xing, L.; Borodin, O.; Chen, H.; Guan, X.; Liu, X.; Xu, K.; Li, W. Improving Electrochemical Stability and Low-Temperature Performance with Water/Acetonitrile Hybrid Electrolytes. *Adv. Energy Mater.* **2020**, *10* (3), No. 1902654.

(15) Dean, J. A. *Lange's Handbook of Chemistry*; McGraw-Hill: 1978. DOI: .

(16) Sui, Y.; Ji, X. Anticatalytic Strategies to Suppress Water Electrolysis in Aqueous Batteries. *Chem. Rev.* **2021**, *121* (11), 6654−6695.

(17) Wang, T.; Sun, J.; Hua, Y.; Krishna, B. N. V.; Xi, Q.; Ai, W.; Yu, J. S. Planar and dendrite-free zinc deposition enabled by exposed crystal plane optimization of zinc anode. *Energy Storage Materials* **2022**, *53*, 273−304.

(18) Xi, M.; Liu, Z.; Wang, W.; Qi, Z.; Sheng, R.; Ding, J.; Huang, Y.; Guo, Z. Shear-flow induced alignment of graphene enables the closest packing crystallography of the (002) textured zinc metal anode with high reversibility. *Energy Environ. Sci.* **2024**, *17*, 3168.

(19) Shi, Z.; Yang, M.; Ren, Y.; Wang, Y.; Guo, J.; Yin, J.; Lai, F.; Zhang, W.; Chen, S.; Alshareef, H. N.; Liu, T. Highly Reversible Zn Anodes Achieved by Enhancing Ion-Transport Kinetics and Modulating Zn (002) Deposition. *ACS Nano* **2023**, *17* (21), 21893−21904.

(20) Zhang, Z.; Xia, S.; Dong, A.; Li, X.; Wang, F.; Yang, J.; Ruan, J.; Li, Q.; Sun, D.; Fang, F.; et al. Mechanical Grinding Formation of Highly Reversible (002)-Textured Zinc Metal Anodes. *Adv. Energy Mater.* **2024**, No. 2403598.

(21) Wang, H.; Li, H.; Tang, Y.; Xu, Z.; Wang, K.; Li, Q.; He, B.; Liu, Y.; Ge, M.; Chen, S.; et al. Stabilizing Zn Anode Interface by Simultaneously Manipulating the Thermodynamics of Zn Nucleation and Overpotential of Hydrogen Evolution. *Adv. Funct. Mater.* **2022**, *32* (48), No. 2207898.

(22) Chen, X.; Li, S.; Wang, K.; Zhao, H.; He, G.; Bai, Y. Halogenated solvation structure and preferred Zn (002) deposition via trace additive towards high reversibility for aqueous zinc-ion batteries. *Energy Storage Materials* **2024**, *73*, No. 103869.

(23) Wang, M.; Wang, W.; Meng, Y.; Xu, Y.; Sun, J.; Yuan, Y.; Chuai, M.; Chen, N.; Zheng, X.; Luo, R.; et al. Crystal facet correlated Zn growth on Cu for aqueous Zn metal batteries. *Energy Storage Materials* **2023**, *56*, 424−431.

(24) Yan, Y.; Shu, C.; Zeng, T.; Wen, X.; Liu, S.; Deng, D.; Zeng, Y. Surface-Preferred Crystal Plane Growth Enabled by Underpotential Deposited Monolayer toward Dendrite-Free Zinc Anode. *ACS Nano* **2022**, *16* (6), 9150−9162.

(25) Li, Q.; Wang, H.; Yu, H.; Fu, M.; Liu, W.; Zhao, Q.; Huang, S.; Zhou, L.; Wei, W.; Ji, X.; et al. Engineering an Ultrathin and Hydrophobic Composite Zinc Anode with 24 μm Thickness for High-Performance Zn Batteries. *Adv. Funct. Mater.* **2023**, *33* (40), No. 2303466.

(26) Zheng, J.; Zhao, Q.; Tang, T.; Yin, J.; Quilty, C. D.; Renderos, G. D.; Liu, X.; Deng, Y.; Wang, L.; Bock, D. C.; et al. Reversible epitaxial electrodeposition of metals in battery anodes. *Science* **2019**, *366* (6465), 645−648.

(27) Zhou, J.; Xie, M.; Wu, F.; Mei, Y.; Hao, Y.; Huang, R.; Wei, G.; Liu, A.; Li, L.; Chen, R. Ultrathin Surface Coating of Nitrogen-Doped Graphene Enables Stable Zinc Anodes for Aqueous Zinc-Ion Batteries. *Adv. Mater.* **2021**, *33* (33), No. 2101649.

(28) Foroozan, T.; Yurkiv, V.; Sharifi-Asl, S.; Rojaee, R.; Mashayek, F.; Shahbazian-Yassar, R. Non-Dendritic Zn Electrodeposition Enabled by Zincophilic Graphene Substrates. *ACS Appl. Mater. Interfaces* **2019**, *11* (47), 44077−44089.

(29) Lee, J. W.; Park, Y. D.; Childress, J. R.; Pearton, S. J.; Sharifi, F.; Ren, F. Copper Dry Etching with Cl2/Ar Plasma Chemistry. *J. Electrochem. Soc.* **1998**, *145* (7), 2585.

(30) Hafner, J. Ab-initio simulations of materials using VASP: Density-functional theory and beyond. *Journal of computational chemistry* **2008**, *29*, 2044−2078.

(31) Ernzerhof, M.; Scuseria, G. E. Assessment of the Perdew−Burke−Ernzerhof exchange-correlation functional. *The Journal of Chemical Physics* **1999**, *110*, 5029−5036.

(32) Perdew, J. P.; Burke, K.; Ernzerhof, M. Generalized Gradient Approximation Made Simple. *Physical Review Letters* **1996**, *77*, 3865−3868.

(33) Grimme, S.; Antony, J.; Ehrlich, S.; Krieg, H. A consistent and accurate ab initio parametrization of density functional dispersion

correction (DFT-D) for the 94 elements H-Pu. *The Journal of Chemical Physics* **2010**, *132*, 154104.

(34) Grimme, S.; Ehrlich, S.; Goerigk, L. Effect of the damping function in dispersion corrected density functional theory. *Journal of Computational Chemistry* **2011**, *32*, 1456−1465.

(35) Kang, L.; Cui, M.; Jiang, F.; Gao, Y.; Luo, H.; Liu, J.; Liang, W.; Zhi, C. Nanoporous CaCO3 Coatings Enabled Uniform Zn Stripping/Plating for Long-Life Zinc Rechargeable Aqueous Batteries. *Adv. Energy Mater.* **2018**, *8* (25), No. 1801090.

(36) Zhao, R.; Wang, H.; Du, H.; Yang, Y.; Gao, Z.; Qie, L.; Huang, Y. Lanthanum nitrate as aqueous electrolyte additive for favourable zinc metal electrodeposition. *Nat. Commun.* **2022**, *13* (1), 3252.

(37) Gomes, A.; da Silva Pereira, M. I. Zn electrodeposition in the presence of surfactants: Part I. Voltammetric and structural studies. *Electrochim. Acta* **2006**, *52* (3), 863−871.

(38) Yang, C.; Zhang, Z.; Tian, Z.; Lai, Y.; Zhang, K.; Li, J. Effects of various carboxymethyl celluloses on the electrochemical characteristics of zinc anode from an alkaline electrolyte. *Electrochim. Acta* **2017**, *258*, 284−290.

(39) Yuan, D.; Zhao, J.; Ren, H.; Chen, Y.; Chua, R.; Jie, E. T. J.; Cai, Y.; Edison, E.; Manalastas, W., Jr.; Wong, M. W.; Srinivasan, M. Anion Texturing Towards Dendrite-Free Zn Anode for Aqueous Rechargeable Batteries. *Angew. Chem., Int. Ed.* **2021**, *60* (13), 7213−7219.

(40) Grujicic, D.; Pesic, B. Electrodeposition of copper: the nucleation mechanisms. *Electrochim. Acta* **2002**, *47* (18), 2901−2912.

(41) Zhao, Z.; Zhao, J.; Hu, Z.; Li, J.; Li, J.; Zhang, Y.; Wang, C.; Cui, G. Long-life and deeply rechargeable aqueous Zn anodes enabled by a multifunctional brightener-inspired interphase. *Energy Environ. Sci.* **2019**, *12* (6), 1938−1949.

(42) Liu, X.; Wang, G.; Lv, Z.; Du, A.; Dong, S.; Cui, G. A Perspective on Uniform Plating Behavior of Mg Metal Anode: Diffusion Limited Theory versus Nucleation Theory. *Adv. Mater.* **2024**, *36* (9), No. 2306395.

(43) Budevski, E. B.; Staikov, G. T.; Lorenz, W. J. Crystalline Metal Surfaces. In *Electrochemical Phase Formation and Growth*, Alkire, R. C.; Gerischer, H.; Kolb, D. M.; Tobias, C. W. Eds.; Wiley: 1996; pp 9−39.

(44) Kim, M.; Lee, J.; Kim, Y.; Park, Y.; Kim, H.; Choi, J. W. Surface Overpotential as a Key Metric for the Discharge−Charge Reversibility of Aqueous Zinc-Ion Batteries. *J. Am. Chem. Soc.* **2023**, *145* (29), 15776−15787.

(45) Scharifker, B.; Hills, G. Theoretical and experimental studies of multiple nucleation. *Electrochim. Acta* **1983**, *28* (7), 879−889.

(46) Isaev, V. A.; Grishenkova, O. V.; Zaikov, Y. P. Theoretical aspects of 2D electrochemical phase formation. *J. Solid State Electrochem.* **2021**, *25* (2), 689−694.

(47) Ait Layachi, O.; Moujib, A.; Khoumri, E. m. Electrochemical Nucleation and Growth Mechanism of Metals. *Electroanalysis* **2024**, *36* (11), No. e202400115.

(48) Yang, Z.; Lv, C.; Li, W.; Wu, T.; Zhang, Q.; Tang, Y.; Shao, M.; Wang, H. Revealing the Two-Dimensional Surface Diffusion Mechanism for Zinc Dendrite Formation on Zinc Anode. *Small* **2022**, *18* (43), No. 2104148.

(49) Zhu, Y.; Liang, G.; Cui, X.; Liu, X.; Zhong, H.; Zhi, C.; Yang, Y. Engineering hosts for Zn anodes in aqueous Zn-ion batteries. *Energy Environ. Sci.* **2024**, *17* (2), 369−385.

(50) Matthijs, E.; Langerock, S.; Michailova, E.; Heerman, L. The potentiostatic transient for 3D nucleation with diffusion-controlled growth: theory and experiment for progressive nucleation. *J. Electroanal. Chem.* **2004**, *570* (1), 123−133.

(51) Narayanan, A.; Mugele, F.; Duits, M. H. G. Electrochemically Induced Changes in TiO2 and Carbon Films Studied with QCM-D. *ACS Applied Energy Materials* **2020**, *3* (2), 1775−1783.

(52) Liu, G.; Zhang, G. Basic Principles of QCM-D. In *QCM-D Studies on Polymer Behavior at Interfaces*, Liu, G.; Zhang, G., Eds.; Springer: 2013; pp 1−8.